JOURNAL OF AIRCRAFT
Vol. 44, No. 6, November–December 2007

Investigation of Relative Humidity and Induced-Vortex Effects on Aircraft Icing

Egemen O. Ogretim* and Wade W. Huebsch†
West Virginia University, Morgantown, West Virginia, 26506-6103
and
Jim Narramore and Bob Mullins
Bell Helicopter Textron, Inc., Fort Worth, Texas 76101

DOI: 10.2514/1.28794

Two new mechanisms for downstream ice growth (i.e., downstream of the primary ice shape) in aircraft icing scenarios were investigated. The first mechanism is local variation of relative humidity with its potential for water deposition due to supersaturation. The second mechanism is induced-vortex effects due to their potential impact on droplet paths. It was shown that for rough surfaces with an extended period of exposure, relative humidity effects can lead to additional growth. The resultant frost is a sandpaperlike roughness that can severely degrade the aerodynamic performance of the wings. It was also shown that the vortices induced by the existing ice-shape features are capable of altering the droplet paths. As a result, impingements occur beyond the limits predicted by the methods in other icing prediction codes.

Nomenclature

a_x, a_y	=	nondimensional acceleration component in the x and y directions
$a_{\xi'}$, $a_{\eta'}$	=	acceleration component in the ξ' and η' directions
a^*	=	reference value for the nondimensionalization of acceleration
C_p	=	pressure coefficient, $(P - P_\infty)/\frac{1}{2}\rho_{\text{air}} V_\infty^2$
c	=	chord length
D	=	diffusivity of water vapor in air, m^2/s
e, e^*	=	actual and saturation vapor pressure, respectively, mbar
h	=	height of the roughness element
K	=	thermal conductivity of water, $\text{J/m} \cdot \text{s} \cdot \text{K}$
L	=	latent heat of vaporization for water, 2.5×10^6 J/kg
LER	=	leading-edge radius, m
LWC, VWC	=	liquid and vapor water content, respectively, in kilograms of water per cubic meter of air
MVD	=	median volumetric diameter, m
N	=	number of droplets in 1 m^3 of air
P	=	static pressure, Pa (unless otherwise stated)
R_v	=	specific gas constant for water vapor, $461\ \text{J/kg} \cdot \text{K}$
RH_w, RH_{ice}	=	relative humidity with respect to liquid water and ice, respectively
r	=	radius of the droplet, m
S	=	cross-sectional area of a sphere, m^2
s_d	=	separation between two neighboring droplets, m
T	=	static temperature, K
t^*	=	reference value for the nondimensionalization of time
V_∞	=	velocity of the approaching flow
v_x, v_y	=	nondimensional velocity component in the x and y directions
$v_{\xi'}$, $v_{\eta'}$	=	velocity component in the ξ' and η' directions
w	=	mixing ratio of water vapor and dry air
γ	=	ratio of the specific heats
ρ_{air}, ρ_v	=	density of dry air and water vapor, respectively, kg/m^3
ρ_{water}	=	density of liquid water, kg/m^3
ψ	=	stream function

Received 15 November 2006; accepted for publication 25 May 2007.

*Postdoctoral Fellow, Civil and Environmental Engineering Department. Member AIAA.
†Assistant Professor, Mechanical and Aerospace Engineering Department. Member AIAA.

I. Introduction

NUMERICAL simulation of aircraft icing has various applications such as aircraft certification, flight simulator development, and ice-shape prediction [1]. The resulting ice shape in a numerical model depends heavily on the collection efficiency distribution over the exposed airframe surface. Therefore, collection efficiency distribution has vital importance for the accuracy and reliability of the numerical predictions. This distribution varies by time due to the coupling between the changing surface geometry and the flowfield. Because of the complexity of the involved flow phenomena, calculation of the collection efficiency is one of the most difficult steps of ice-accretion prediction.

The calculation of the collection efficiency involves the tracing of the droplets in the flowfield. There are two different approaches for this purpose [2]: Eulerian and Lagrangian. Each of these approaches has its own advantages and disadvantages. Typically, for a two-dimensional computation, it is better to incorporate a Lagrangian approach. As for 3-D computations, the Eulerian approach is preferred, to decrease the computational load and cost.

The droplets that have been used previously in numerical studies usually have less than 40-μm median volumetric diameter (MVD). The smaller among these droplets are expected to follow the streamlines reasonably well. The larger ones, however, impinge on the wing surface due to their high inertia and form ice. For either case, a droplet tracing is necessary to predict the consequences. To compute the droplet trajectory, the following assumptions are generally used [3]:

1) Flowfield and the droplets are decoupled, and so the droplets do not alter the flow.

2) The droplet radius remains constant until it hits the surface, hence constant droplet water content.

3) The splashing effects are negligible and so there is not a redistribution of water after splash.

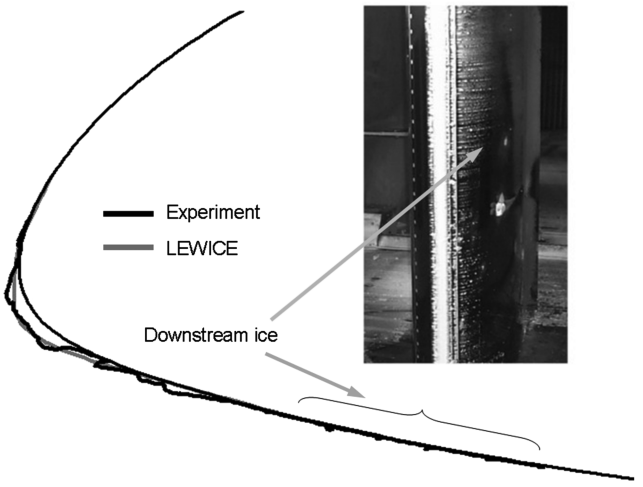

Fig. 1 A photograph and the plot of the experimental data, with the LEWICE prediction for the same case, to show the downstream ice phenomenon.

4) The droplets are assumed to have a spherical shape for drag computation purposes.

The extended research and in-flight observations have shown that there are situations in which the predicted shapes cannot account for the ice growth downstream of the primary ice shape, such as shown in Fig. 1. Especially in mixed-phase clouds, droplets of much larger size can be encountered [3]. The MVD for these droplets can be on the order of 100 μm. These droplets do not comply with the aforementioned assumptions and cause unpredictable ice shapes due to different underlying mechanisms. An example of the unpredictable features of the resultant ice shapes is the feather growth, which takes place beyond the calculated impingement region [4]. As the feathers grow, not only do they distort the oncoming and downstream flow, but they also constitute an added impingement region that protrudes into the flow. Therefore, droplets that bypass the stagnation area can be important due to their contribution to ice growth downstream [4]. This shows clear evidence for the necessity of accurate droplet trajectory calculations and for the importance of completeness of the water transport models.

Currently, the effects of relative humidity on water transport are neglected in ice-accretion prediction, considering that "it is at best a secondary effect" [5]. However, a previous study [6] showed that although there is a negligible effect for the primary ice shape, there is a potential for the relative humidity to impact the downstream ice growth due to local supersaturation. It was reported that depending on the time scales and the level of subsaturation and/or supersaturation, the liquid water distribution on the wing surface can be affected. The same study outlines the steps for calculating the relative humidity field for a given flowfield. Therefore, an alternative mechanism for downstream ice growth is the local variations of relative humidity.

Another potential mechanism for downstream ice growth is the change of droplet paths due to viscous effects. In many of the current ice-accretion prediction codes, potential flow is used as the basis for the droplet trajectory calculations. Because of their inviscid character, potential flow solvers cannot capture some critical flow phenomena. For example, vortex shedding, triggered by the growing ice roughness, can cause droplet impingements on surfaces that are beyond the impingement limits predicted based on potential flow.

The present work is a follow-up study on relative humidity effects and induced-vortex interaction as mechanisms for downstream ice growth (i.e., ice formation beyond the primary leading-edge ice shape). The preliminary studies on these mechanisms [6,7] include the local relative humidity variation in the flowfield around an experimental rime ice shape, the time scales associated with the processes triggered by relative humidity, the consequence of relative humidity changes on droplet diameter, and droplet tracing in a temporal snapshot from an unsteady flowfield over an experimental glaze ice shape.

The present study includes further explanation of the formulations related to the relative humidity calculations with a more comprehensive parameter set. For example, the latent heating/cooling and the subsequent air expansion/compression are added to the previous box model in [7]. Also, droplet tracing in a fully unsteady flow is presented to investigate the interaction between the droplets and the induced vortices. Finally, an approximation for the amount of extra water deposition due to relative humidity and induced-vortex interaction is given.

The key findings of the present study are that given enough time, relative humidity can cause sufficient water phase change that can double the liquid water content (LWC) in the air. In a particular case, the local supersaturation led to $\sim$0.4-mm growth of the existing roughness over a 30-min period; the vortices induced by the existing ice-shape features were strong enough to divert the droplet paths, causing downstream impingements. In a particular case, there were 6.5% extra impingements due to droplet interaction with these vortices, which led to a 0.24-mm-thick water layer in 7 min along 10% chord behind the primary glaze ice horn.

II. Governing Equations

The in-house flow solver that is used in this study is a 2-D unsteady incompressible solver with a stream-function/vorticity formulation. The boundary conditions are no-slip at the solid boundary, Blasius profile at the far downstream, and inviscid condition at the far upstream. The stream function and vorticity transport equations, originally in Cartesian coordinates, are taken through multiple transformations to arrive at the final governing equations. These transformations are performed for several reasons: 1) to produce an orthogonal body-fitted grid, 2) to account for the surface roughness within the governing equations, and 3) to implement stretching and clustering of the grid lines for flow resolution. The first transformation uses conformal mapping to cast the governing equations in a parabolic coordinate system, which produces a body-fitted grid. The surface roughness is introduced through the use of a Prandtl transposition (or shearing transformation) similar to the work of Huebsch and Rothmayer [8]. The numerical scheme is fully implicit finite differencing in 2-D. Further discussion of the solver and the related equations for flowfield calculations are left to [6,8,9], for brevity. Also, the final governing equations (after transformations) for this study are included in the Appendix for interested readers.

A structured grid is used with a high resolution in the leading-edge region. A typical grid structure is provided in Fig. 2, which is a body-fitted grid around an airfoil with a rime ice shape on the leading edge. Typical grid sizes for this study were 4001×201 grid points in the streamwise and normal directions, respectively. A majority of these

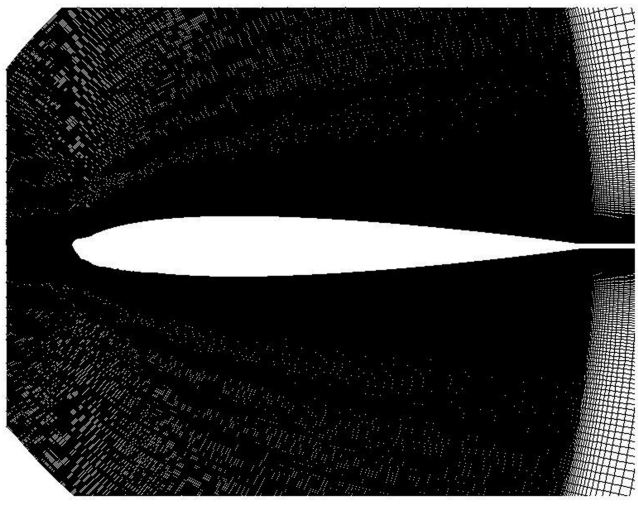

Fig. 2 Typical body-fitted grid for the leading-edge rime ice case.

grid points are clustered in the leading-edge region and near the wall. Grid independence studies have been conducted in previous work for similar flight Reynolds numbers and surface geometries [8], and so those results have been applied to the working grids of the current study.

The auxiliary equations that are employed in this study are grouped under two main categories: relative humidity and droplet tracing. The equations are referenced back to previous literature when possible. Only the new aspects and methods are discussed in detail here.

A. Relative Humidity

There are two main parameters that determine the level of relative humidity (i.e., saturation level): the amount of water vapor present in the air and the maximum amount of vapor that air can hold at the local saturation conditions, which is a function of local pressure and temperature. Relative humidity is defined based on the final phase in the relevant phase change: relative humidity with respect to liquid water (RH_w) and relative humidity with respect to ice (RH_{ice}). In terms of RH_w, a supersaturation will cause condensation to liquid phase, whereas a subsaturation will favor evaporation to vapor phase. Similarly, in the case of RH_{ice}, a supersaturation will cause deposition to solid phase, whereas a subsaturation will cause sublimation to gas phase. It should be noted that even if the ambient conditions are subsaturated with respect to liquid water, there still could be supersaturation with respect to ice. However, it is also likely that a supersaturation with respect to both liquid water and ice are present in the flowfield over the wing. In this case, the effects of both saturations will be observed, but condensation has a shorter time scale. Any of these phase changes due to relative-humidity-related mechanisms will result in a subsequent change in local thermodynamic properties.

In the present work, an updated time-scale study was performed. The effect of initial droplet diameter and the ambient relative humidity on the time scales for the relative humidity induced processes were investigated, with a more complete and accurate model compared with the model of [7]. In addition to the time-scale study, an estimation of the upper limit for the amount of condensate was made to determine the merit of the relative humidity compared with other factors in aircraft icing.

Before going into the relevant investigations, it is necessary to discuss the use of the isentropic relation for relative humidity calculations as opposed to the ideal gas relation, even for an incompressible flow. The isentropic relation accounts for changes in density, whereas the flows that are considered in engineering applications do not always have compressibility effects. So is it acceptable to use the ideal gas relation to obtain temperature from pressure with assumed constant density? Or is it essential to use the isentropic relation? For the present work, the answer to this question is that the isentropic relation is essential for the relative humidity calculations to pass from the pressure field to the temperature field. The underlying logic is similar to that under the Boussinesq approximation [10]. Very small changes in density can store or release enough energy that can cause significant change in the saturation level, though the incompressible assumption may still be reasonable. If minor changes in density are ignored, significant error can be incurred in the relative humidity calculations. Figure 3 demonstrates the growth of error in the calculation of relative humidity as a function of drop in pressure. For a C_p value of -3, there is $\sim$80% difference between the two results.

1. Box Model

The box model of [7] was used with its updated form to investigate the two issues of time scales and available excess water. The numerical simulation that was performed [7] includes the following steps. A sudden temperature change is imposed isentropically on the control volume, which also changes the pressure. The change in pressure alters the saturation level of the system, which was initially set to be 100% (saturated) with respect to liquid water. What is expected is that due to the condensation of the vapor or evaporation of the droplets within the control volume, the system will come to a new equilibrium condition. In this new equilibrium, the relative humidity will again be 100% with respect to liquid water at the imposed pressure level.

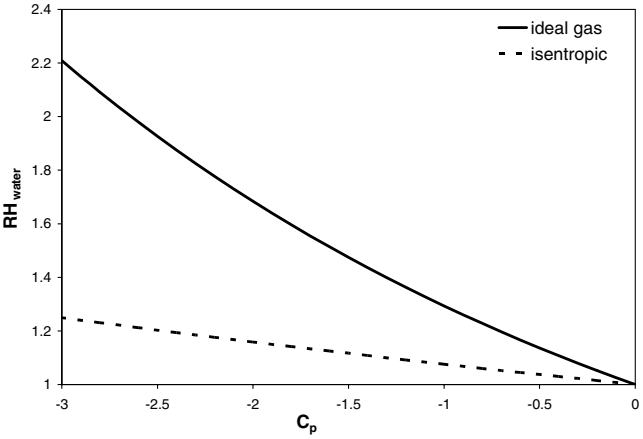

Fig. 3 Comparison of variation of RH_w as given by ideal gas and isentropic relations; values are calculated for 21-in. chord length and 5000-m altitude in standard atmosphere; $Re_c = 1 \times 10^6$.

During this process, the droplet radius and LWC are recorded as a function of time until a specified convergence criterion is met. The same basic methodology of [7] is used for the calculation of the relative humidity effects on the droplets, with some changes and additions [11]. The primary change is the use of the isentropic relation to calculate the temperature from the pressure in the chamber. The additions are the latent heating/cooling effect due to phase change and the subsequent volume change of the container. The final methodology is given in the Appendix.

To approximate the upper limit of the relative humidity effects, a simple calculation was made to see the amount of excess water in case of supersaturation at different levels. The amount of excess water changes as a function of the local drop in temperature and pressure, hence the local increase in relative humidity, compared with the ambient flow. An important point to note here is that higher velocities will cause higher drops in the actual pressure and temperature in the flowfield, which means more excess water. Therefore, the available excess water is a function of the Reynolds number governing the flow as well. The amount of excess water was found simply by using the difference between the amount of vapor present at the initial conditions and at the new equilibrium, as shown next:

$$m_{\text{available vapor}} = V^* \rho^*_{\text{air}} (w_{\text{initial}} - w^*_{\text{imposed}}) \tag{1}$$

where $w = [0.622e/(p - e)]$.

2. Surface Roughness Growth

Regardless of the extent of the time of relative humidity processes, for every parcel of air passing through the supersaturated regions, there will be some level of condensation. This condensate can accrete to considerable amounts when integrated over a long exposure. To make an estimate of this effect, the numerical simulation of the box model was used, with some modifications for flight at 5000-m standard atmosphere with $Re_c = 1 \times 10^6$ and 21 in. of chord length. For a reference length, the portion between 10 and 30% chord locations was chosen. There are two reasons for this choice:

1) This area corresponds to the downstream ice roughness observed behind the main ice shape.

2) This area is typically under very low pressure, even for clean airfoils.

The XFOIL [12] program was used to calculate the pressure distribution around a NACA 0012 airfoil at a 4-deg angle of attack. The average pressure was calculated in the mentioned portion of the airfoil, both on the upper and on the lower surfaces, separately. An estimate of magnitude of the velocity for this average pressure was

calculated using the Bernoulli equation, which along with the reference length ($0.2c$) gives an estimate of the average residence time for the droplets in this supersaturated region. The change in local pressure and temperature alter the relative humidity level, which leads to phase change from the vapor to liquid water. Within the given residence time, the change of LWC was determined by using the formulation in the Appendix, then the region was refreshed by the next volume of air. This procedure continued for a prescribed accretion time. The surface roughness elements were initially set to have the same radius (MVD/2) as the droplets in the air. This means that there is an initial level of ice crystal roughness on the surface. The height of these surface roughness elements continuously increases due to the continuous condensation.

B. Droplet–Vortex Interaction

The Lagrangian particle tracing in this study is a postprocess that inputs a flowfield solution from the 2-D Navier–Stokes flow solver [8,9]. The advantage of this approach is that the effects of the local flow dynamics in the leading-edge region, such as a separation bubble or unsteady vortex shedding, are revealed. As a result, the impact on droplet collection efficiency outside of "potential flow impingement limits" can be investigated. The forces acting on a particle (in this case, a water droplet) and the subsequent acceleration were calculated according to the following subsections:

1. *Drag Force*

The drag coefficient acting on the spherical droplet was calculated by the following formula [10]:

$$C_{d_{\text{sphere}}} = \frac{24}{Re} + \frac{6}{1+\sqrt{Re}} + 0.4 \quad \text{for} \quad 0 \le Re \le 2 \times 10^5 \tag{2}$$

where $Re = (2Ur/v_{\text{air}})$.

In the definition of the Reynolds number, the speed of the flow is relative to the droplet. In this case, both the droplet and the flow have speeds as a function of time and space. Therefore, the relative speed of the wind with respect to the sphere needs to be calculated. The drag force acting on the spherical droplet was then calculated from the drag coefficient.

2. *Gravity and Buoyancy*

Gravitational force exhibits itself in the negative y direction and is constant in the computational field. The buoyancy force acts in the positive y direction and is constant, due to the incompressible character of the flow solver. Although it is negligible in magnitude, the following formula is used for the buoyancy force:

$$F_{\text{buoyancy}} = -m_{\text{droplet}} \frac{g(\rho_{\text{water}} - \rho_{\text{air}})}{\rho_{\text{water}}} \tag{3}$$

3. *Calculation of the Velocity and Acceleration*

The velocities are calculated in the transformed ξ'–η' plane (a characteristic of the flow solver [8,9]). The flowfield velocity components are calculated by Eq. (4). More details can be found in the Appendix.

$$v_{\xi'} = \frac{\mathrm{d}\psi/\mathrm{d}\eta'}{h} \qquad v_{\eta'} = -\frac{\mathrm{d}\psi/\mathrm{d}\xi'}{h} \tag{4}$$

where $h = \sqrt{\xi'^2 + \eta'^2}$.

Therefore, the velocity difference between the droplet and the local flow can be readily calculated in the transformed plane. The calculation of the accelerations, however, is more difficult because the relevant force calculations require a transformation between two different planes (x–y and ξ'–η'), due to the character of the flow solver. The magnitude of the drag requires the magnitude of the velocity, and the force due to gravity and buoyancy are acting in the y direction. Therefore, the magnitude of the velocity and these forces needs to be expressed in both planes.

The transformation function [13] between the two planes is

$$x = \frac{\xi'^2 - \eta'^2}{2} \qquad y = \xi'\eta' \tag{5}$$

Then, by making use of the differential geometry rules (see the Appendix), the following are found:

$$|V|^2_{x-y\ \text{plane}} = h^2 |V|^2_{\xi'-\eta'\ \text{plane}} \tag{6}$$

The acceleration terms are obtained by simply taking the second derivative of the corresponding coordinate with respect to time:

$$\begin{aligned} a_{\xi'} &= [\xi' a_x + \eta' a_y - \xi(v_\xi^2 - v_\eta^2) - 2\eta v_\xi v_\eta]/h^2 \\ a_{\eta'} &= [\xi' a_y - \eta' a_x + \eta(v_\xi^2 - v_\eta^2) - 2\xi v_\xi v_\eta]/h^2 \end{aligned} \tag{7}$$

where a_x and a_y are the nondimensional acceleration components in the x and y directions, respectively, calculated from the forces acting on the droplet.

One last point is that the formulation of the flow solver involves some nondimensionalization, which is also reflected on the calculation of the acceleration and velocity components. The velocity is nondimensionalized by the far upstream flow speed V_∞, and the time is nondimensionalized by using the ratio of the leading-edge radius LER and V_∞. Therefore, the acceleration terms appearing in Eq. (7) are nondimensional terms obtained by the characteristic acceleration, given next:

$$a^* = \frac{V^*}{t^*} = \frac{V_\infty}{(\text{LER}/V_\infty)} = \frac{V_\infty^2}{\text{LER}} \tag{8}$$

4. *Numerical Approach for the Local Values*

The calculation of the drag force and the subsequent acceleration depends on the velocity difference between the droplet and the local wind. Because the droplet can be located at a point within the grid cell, the relevant acceleration calculations require an interpolation to determine the local wind speed. The generic interpolation function used in the present study assumes a rectangular cell (see Fig. 4) and determines the intermediate values as follows:

$$\begin{aligned} u_{\text{local}} &= u_{ll} + \frac{\partial u}{\partial \xi'}\Delta\xi' + \frac{\partial u}{\partial \eta'}\Delta\eta' \\ &= u_{ll} + \frac{u_{lr} - u_{ll}}{\xi'_{lr} - \xi'_{ll}}(\xi'_{\text{droplet}} - \xi'_{ll}) + \frac{u_{ul} - u_{ll}}{\eta'_{ul} - \eta'_{ll}}(\eta'_{\text{droplet}} - \eta'_{ll}) \end{aligned} \tag{9}$$

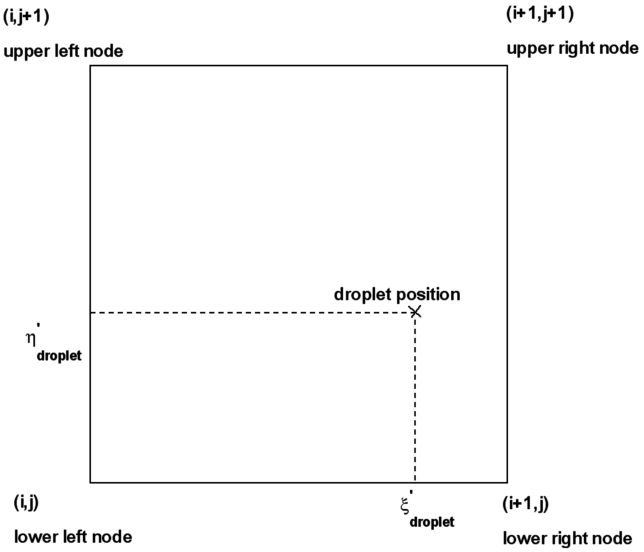

Fig. 4 Sketch for the interpolation of the local flow velocity for the calculation of the drag force acing on a droplet that is located at an intermittent point in the grid cell.

Table 1 The values for *n*, number of spanwise repetitions, and the corresponding LWC

MVD, μm	n	Spanwise repetitions	LWC, g/m^3
20	3	493	0.50
30	4	370	0.71
40	6	246	0.50
50	7	211	0.62

5. Calculation of LWC for the Simulated Unsteady Flow

The calculation of LWC involves two assumptions: uniform droplet distribution in the given volume and uniform droplet diameter, which is kept constant during the calculations. The temporal frames that were obtained from the simulation of the unsteady vortex field were 32.2 μs apart. For a continuous droplet tracing in the unsteady process, droplets must be released at integer multiples of this time gap. Therefore, the separation between two consecutive droplets, s_d, is given by $s_d = V_\infty(32.2x10^{-6}n)$, where n is a prescribed integer (see Table 1). The same length is also used to calculate the number of repetitions of the two-dimensional case in the spanwise direction. So the number of repetitions for the unit span is $1/s_d$ and is also shown in Table 1. The only criterion when selecting the value of n is that the calculated LWC value must be in the range that is used in the icing-tunnel experiments. This range is roughly between 0.3 and 1.6 g/m^3.

Given that there is a uniform droplet distribution in the unaffected flow, the distance between two neighboring droplets in all three dimensions of space is going to be s_d. Then every droplet is contained in a cube of volume s_d^3, which relates to the total number of droplets in a unit volume by $N = s_d^{-3}$. The amount of liquid water in a unit volume of air, which is LWC, can be calculated by multiplying the number of droplets N with the mass of a single droplet, as shown in Eq. (10). The calculated values of LWC for the cases considered in the present study are given in Table 1.

$$\text{LWC} = Nm_{\text{droplet}} = N\left[\frac{4}{3}\pi\left(\frac{\text{MVD}}{2}\right)^3\rho_{\text{water}}\right] \tag{10}$$

III. Results

The results in this study include two parts, each addressing a different mechanism in downstream ice growth.

A. Relative Humidity

Several aspects of the relative humidity effects are presented in this section based on the improved results.

1. Relative Humidity Field

With the improved formulation, a flowfield analysis was made on a NACA 0012 airfoil with experimental glaze ice at a Reynolds number of 5×10^5 based on chord. The subsequent pressure field and the corresponding relative humidity levels with respect to liquid water were calculated (Fig. 5) based on this flowfield, which was initially set to be saturated at the unaffected conditions. The low pressure on the suction surfaces and the unsteady vortex shedding from the ice roughness induce highly supersaturated conditions over the airfoil and ice surface. Aside from surface effects, the vortex cores have the potential to act as nests for ice or droplet growth.

2. Available Excess Water

The amount of available excess water in 1 m^3 of air is plotted against the relative humidity with respect to liquid water in Fig. 6. Although not shown, as higher levels of supersaturation are achieved, this curve asymptotically approaches 1.32 g/m^3, which is the total amount of water vapor in the 100% saturated air of unit volume at 5000-m altitude for standard atmosphere conditions.

The actual pressure distribution on an airframe indeed varies with the Reynolds number. Higher Reynolds numbers cause higher drops in pressure over an airfoil surface and therefore can more abruptly achieve the high relative humidity values, compared with the lower Reynolds numbers. This phenomenon is depicted in Fig. 7 for saturated air at 5000-m altitude in standard atmosphere. The relative humidity of this air changes according to the variations in pressure and temperature, which can occur due to the passage of an aircraft wing. Assuming a C_p value of -2, the new relative humidity value and the excess amount of water in a unit volume of air was calculated for different flow speeds. As the Reynolds number increases, the excess amount of water vapor in the air exponentially increases. This figure follows the excess water up to 0.6 g/m^3. However, the curve eventually assumes an S shape and asymptotically approaches the same 1.32 g/m^3 value as higher Reynolds numbers are achieved for the same nondimensional pressure.

For the icing experiments in wind tunnels, the LWC values are usually between 0.3–1.6 g/m^3. The values of excess water vapor shown in Figs. 6 and 7 are comparable to the amount of liquid water used in the experiments. This shows that if the mechanisms involved in the ice-accretion process interact with this excess water vapor, it can be expected that the resultant ice accretions will be different from the predictions that ignore relative humidity interactions.

3. Time Scales

The objective of this part of the study was to establish whether the residence time of the vapor-air mixture within the supersaturated regions was sufficient for any relative humidity induced effect to occur. The box-model simulation was performed for the investigation of the time scales in a stationary case [7] with the aforementioned changes and additions. Figure 8 shows the LWC history for different initial relative humidity levels with respect to liquid water. The initial diameter of the droplets was 10 μm for this case. As seen in this figure, the imposed level of relative humidity at the start of the simulation did not affect the time required to

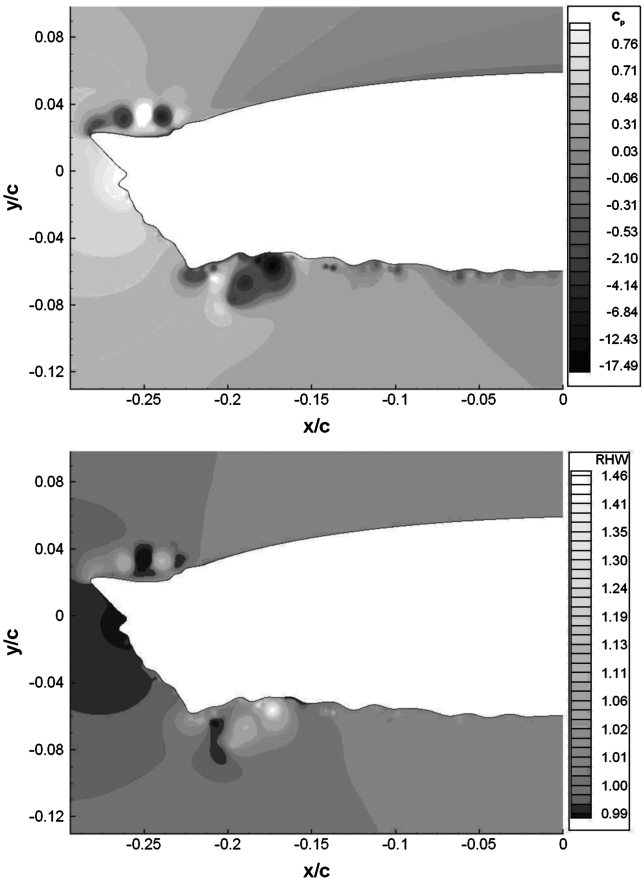

Fig. 5 Pressure field and the corresponding relative humidity levels with respect to liquid water for a NACA 0012 airfoil with experimental glaze ice accretion; $Re_c = 5 \times 10^5$.

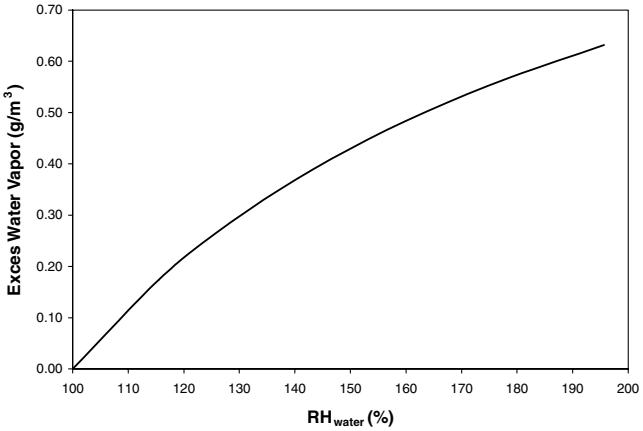

Fig. 6 Variation of excess water vapor mass as a function of relative humidity with respect to liquid water; values are calculated for 5000-m altitude in standard atmosphere.

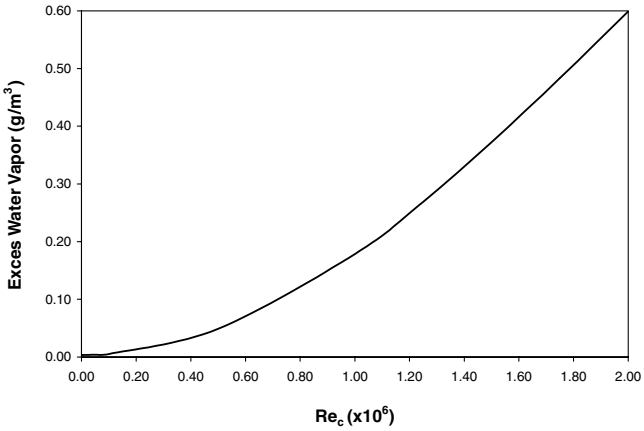

Fig. 7 Variation of excess water vapor as a function of Reynolds number; values are calculated at $C_p = -2$ for a chord length of 21 in. at 5000-m altitude in standard atmosphere.

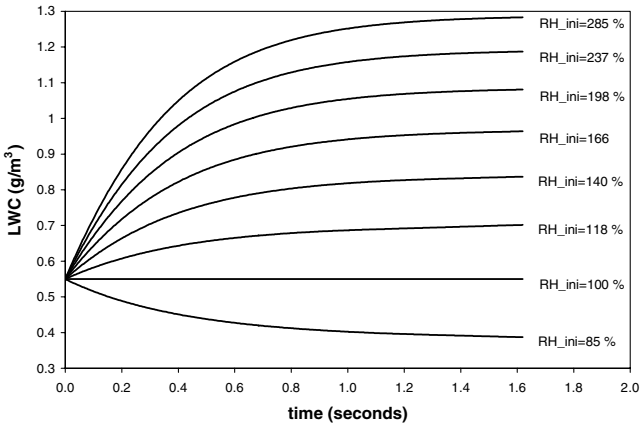

Fig. 8 LWC history for different initial relative humidity levels.

reestablish the equilibrium conditions. For all cases, the equilibrium recovery time was 1.6 s. However, as expected, the initial relative humidity level determines the final LWC at the equilibrium conditions, in which relative humidity is again 100%. For the droplets with 10-μm diameter, given sufficient time, the relative humidity has the potential to increase the LWC in the flow as much as 100% or to decrease it 30%. However, the required time to complete this process is too long when compared with the residence time of air over the leading edge of a wing in actual flight conditions.

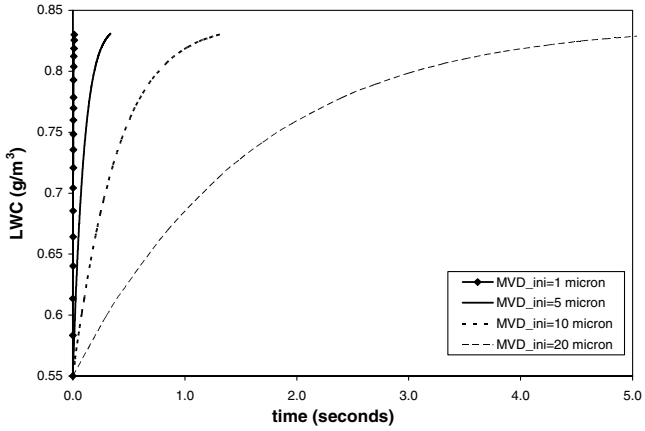

Fig. 9 LWC history for different initial MVDs; imposed initial $\mathrm{RH}_w = 140\%$.

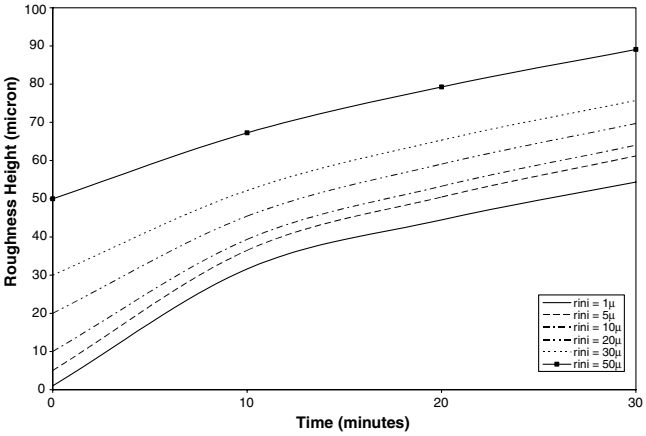

Fig. 10 Change in roughness height due to relative humidity on the upper side of a NACA 0012 airfoil in-flight with $Re_c = 1 \times 10^6$ at 5000-m standard atmosphere.

Further investigation of the time scales was done by keeping the initial relative humidity constant at 140% and varying the initial diameter of the droplets present in the air. It was seen that the size of the droplets has a large impact on the time required for the relative-humidity-induced condensation process (Fig. 9). By reducing the size of the droplets from 20 to 1 μm, the duration of the process was reduced from 5 s to 12 ms. This means that a portion of the droplets that are seen in actual icing scenarios, which are as small as 6 μm, are much more vulnerable to the relative humidity effects when compared with larger droplets. As a result of this variation in vulnerability, the droplet spectrum is further smoothed such that the smaller droplets grow in size.

4. Surface Roughness Growth

The results of this numerical experiment are presented in Fig. 10 for the upper surface ($C_{p,\text{average}} = -0.72$ and $\mathrm{RH}_w = 105.41\%$) and in Fig. 11 for the lower surface ($C_{p,\text{average}} = -0.05$ and $\mathrm{RH}_w = 100.37\%$) of a NACA 0012 airfoil. Note that the specified local relative humidity values above 100% are due to the fact that the moist air is in a transient state as it flows over the airfoil with high speed. In both Figs. 10 and 11, it is seen that the initial rate of growth is higher for the roughness elements with smaller radii. However, as they grow in size, the growth rate of all roughness elements reaches about the same value. Over a 30-min period, the roughness elements on the upper side, which were initially 50 μm in diameter, grew to a diameter of 90 μm due to the local supersaturated conditions. This level of roughness is sufficient to cause an increase in drag; for further extended exposures, it is likely to form new impingement surfaces beyond the direct-impingement region on the leading edge. On the

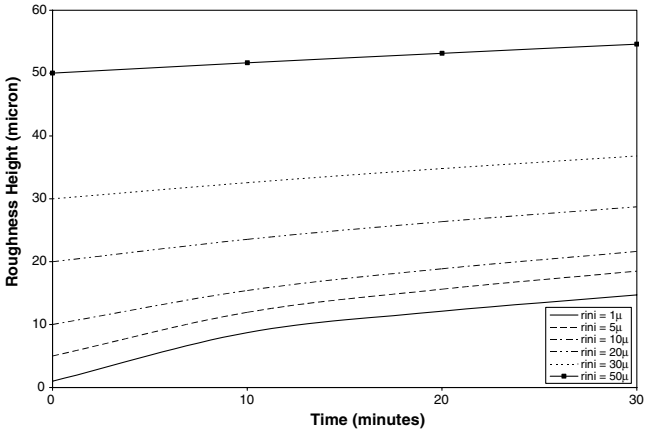

Fig. 11 Change in roughness height due to relative humidity on the lower side of a NACA 0012 airfoil in-flight with $Re_c = 1 \times 10^6$ at 5000-m standard atmosphere.

lower side, due to a lower degree of supersaturation, the condensed amount was less, as reflected by the 5- to 10-μm increase in the diameters of the roughness elements located therein. In previous literature, roughness at this level ($h/c = 10^{-4}$) is associated with a decrease in maximum lift as much as 13% and increase in drag up to 40% [14,15], depending on its location.

As an interim conclusion, it can be said that within the direct-impingement region, the effect of the relative humidity is not likely to be seen. This is because the high amount of water coming with the droplets will suppress the effects manifested due to relative humidity. However, the areas that are out of direct impingement (e.g., the rear side of the large roughness elements and suction surfaces beyond the direct-impingement limits) are still subject to supersaturation for prolonged periods. So there is potential that condensation and frost growth will be induced in these regions due to relative humidity effects.

B. Vortex Interaction

In typical ice-accretion codes, droplets are subject to the flow induced by the potential flow coupled with a boundary layer solver. This type of solver is not capable of capturing the unsteady separation and vortex dynamics and the resulting interaction with the flow. The unsteady Navier–Stokes solver used in the present study is capable of capturing large- and small-scale flow features, including separation bubbles and vortex shedding. These vortex structures may alter the path of the droplet. Consequently, a droplet may impinge on a location other than the one predicted by the potential flow solver, or a droplet that is calculated to bypass the surface may impinge. An example of this phenomenon was investigated for an unsteady flow over a NACA 0012 airfoil with experimental glaze ice [16]. Although in the droplet-tracing process the unsteady flowfield is used, the stream function contours at a snapshot in time from the vortex-shedding process are given in Fig. 12 to give an idea about the level of activity in the aft region of the glaze ice.

At each designated time step, a certain number of droplets were released from the same initial locations. The designated time steps were chosen such that the distance between the neighboring droplets is the same both vertically and horizontally in the approaching flow. Although the consecutive droplets started from the same initial locations, their paths were not necessarily the same if they interacted with the unsteady features.

For the droplets that impinge the frontal area of the ice shape, the paths due to successive droplets from the same original point overlap because they are not interacting with the unsteady features of the flow. It is important to note here that in an actual case, the droplets would be distributed randomly with some average distance between them, rather than aligning themselves on a grid. As for the droplets that penetrate into the rear regions of the glaze ice, they interact with the unsteady features of the flow. Therefore, the paths of the droplets released from the same location do vary due to the unsteady effects in

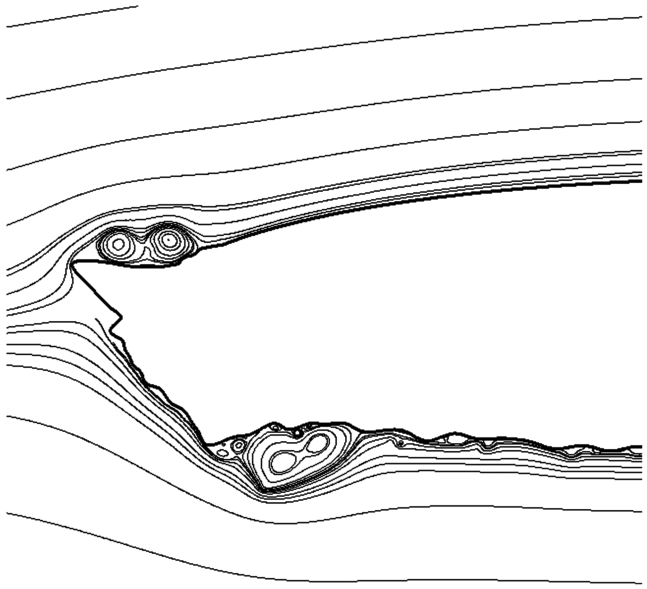

Fig. 12 Stream function contours around a NACA 0012 airfoil with glaze ice showing the shed vortices.

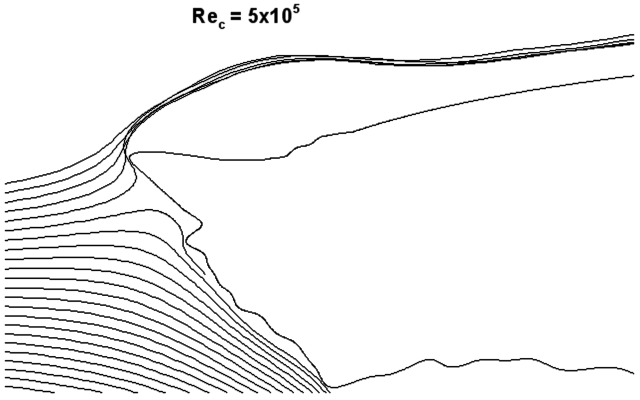

Fig. 13 Paths of the droplets (MVD = 5 μm) that are released simultaneously in an unsteady flow around a NACA 0012 airfoil with glaze ice.

the rear of the glaze horn. The crucial point in these tracing summaries is that the rear impingements would not be seen by the ice-accretion prediction codes that rely on potential flow for droplet tracing. This means that the potential for additional ice growth beyond impingement limits is physically absent in the formulation of these codes.

A parametric study of the effect of droplet size was made using this unsteady flow. The droplets with varying diameter were traced in a flow at 5×10^5 Reynolds number for a 21-in. chord, and 5000-m altitude in standard atmosphere. The first set of droplets with the smallest diameter of 5 μm followed the streamlines very closely so that none impinged on the surface (see Fig. 13). Even the droplets that were heading for the frontal area of the glaze ice slowed down and followed the local air, no matter how curved the resultant paths were. It is important to note here that such a result is the case for these small droplets at the specified Reynolds number. A change in the droplet size and/or a change in the Reynolds number would reveal a different picture in which the droplets could impinge the frontal area. As a matter of fact, the next bigger size of droplets considered in this study at the same Reynolds number did impinge on the frontal area of the ice shape, as seen in Fig. 14.

The rest of the tests contained droplets with 20-, 30-, 40-, and 50-μm diameters. Each set was run through the unsteady field separately and the paths of all of the droplets that impinged the surface were superimposed and are shown in Figs. 14–17. For the

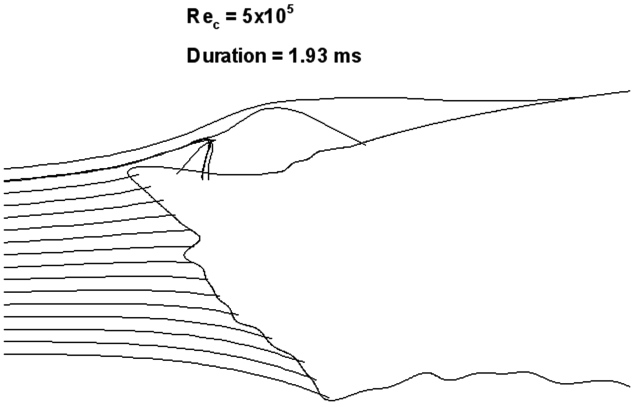

Fig. 14 All droplet impingement paths (MVD = 20 μm) in an unsteady flow around a NACA 0012 airfoil with glaze ice.

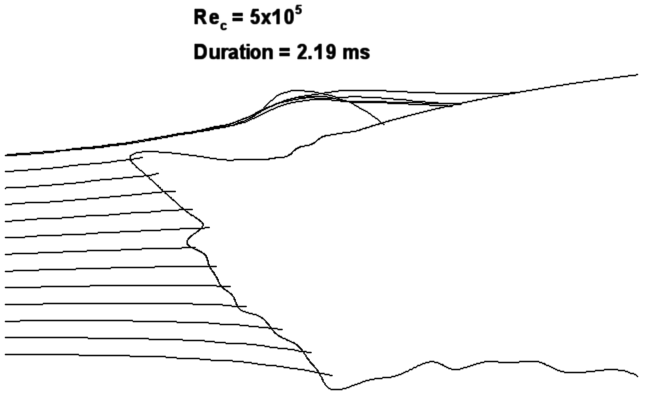

Fig. 15 All droplet impingement paths (MVD = 30 μm) in an unsteady flow around a NACA 0012 airfoil with glaze ice.

20-μm case (Fig. 14), the vortex behind the glaze horn causes strong divergence from the regular path, because the inertia of the droplet is low enough that its path is easily manipulated. The same trends were observed at different phases of the unsteady vortex shedding for droplets with 30-μm (Fig. 15) and 40-μm (Fig. 16) diameters. However, for the 50-μm case, the shed vortices were never strong enough to cause severe change in path, though they still caused slight deviation leading to impingement.

As expected, these results show that the inertia of the droplet must be relatively low compared with the strength of the vortices so that their effects can impact the subsequent paths of the droplets. The two extremes of the droplet inertia/vortex strength comparison are droplets with very high inertia and the droplets with very low inertia. For a droplet to exhibit the vortex interaction effects, it must have low enough inertia to get into the interaction with the vortices, but, at the same time, high enough inertia to end up with an impingement with the surface.

Table 2 shows the MVD of the droplets that were used in the simulation, with the corresponding number of impingements recorded on the frontal area of the main ice shape and on the rear side of it. The frontal impingements are those that can also be captured by the particle-tracing programs that are based on potential flow

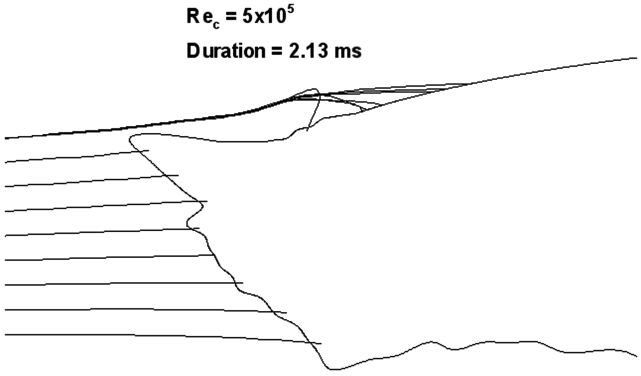

Fig. 16 All droplet impingement paths (MVD = 40 μm) in an unsteady flow around a NACA 0012 airfoil with glaze ice.

calculations, because these droplets do not interact with the induced vortices. However, the rear impingement events cannot be captured by typical ice-accretion codes, because there is a clear interference due to the unsteady vortex shedding.

To make an estimate of the corresponding extra thickness of the accumulated water, an exposed surface area was chosen with dimensions of 1 m along the wing span and 10% chord length ($c = 21$ in.). The reason for choosing 10% chord length is that in icing experiments, the minor ice roughness extends around 10–15% chord length behind the main ice shape. Using the number of additional impingements in Table 2, the total number of impingements over a 7-min period (common for experimental icing tests) was calculated. Note that this calculation is based on the assumption that the acquired statistics provides a good enough sample for the actual physics. The amount of liquid water accreted due to the extra impingements in this period was obtained by multiplying the total number of impingements with the volume of a single droplet. Then this total volume of liquid water was assumed to be spread over the surface area mentioned earlier.

The case with 20-μm MVD had the least impact, with 0.06 mm of extra water-layer accumulation due to the vortex-induced impingements. This was mainly due to the diameter of the droplets. The droplet mass, hence the water content of the droplets, increases with the cube of the diameter. The highest level of impact came with the 50-μm droplets, with an extra water layer of 0.24 mm in 7 min.

The droplet tracing in this study was done for a 2-D flow over a NACA 0012 airfoil with glaze ice. However, it is obvious that a true picture of the flow physics over complex ice geometry involves several 3-D aspects, such as the other two components of the vortices, and vortex stretching. These must be considered for a better understanding of the droplet–vortex interaction. In addition, to enhance the statistical accuracy, the considered period of unsteady flow can be extended. It is also desirable to see how these induced vortices interact with the surface water that forms due to the affected droplets by the induced vortices. Considering a wide range of Reynolds numbers and roughness features will help determine the significance of these mechanisms in terms of ice accretion at different speeds. In addition, there is a need for experimental verification of this mechanism by using high-speed video camera recordings of the ice-accretion experiments with a focus on the aft region of the main ice shape. These will help to better understand the behavior of the droplets in this region and the motion of the water on the airfoil surface. All of the mentioned improvements may help to understand

Table 2 Statistics of the interaction of the unsteady vortex field with the droplet paths

		Number of impingements		
MVD, μm	Duration, ms	Front	Rear	Extra thickness in 7 min (mm of water for 0.1c, unit span)
20	1.93	294	7	0.06
30	2.19	216	5	0.09
40	2.13	108	7	0.21
50	2.25	88	5	0.24

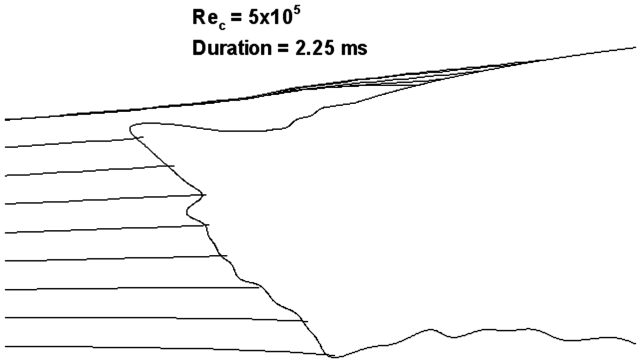

Fig. 17 All droplet impingement paths (MVD = 50 μm) in an unsteady flow around a NACA 0012 airfoil with glaze ice.

how the rime feathers and other roughness features beyond the glaze horn relate to these new mechanisms.

IV. Conclusions

This study focused on two main alternative mechanisms for downstream growth of ice shapes over the critical aircraft surfaces. These mechanisms are the relative-humidity-induced ice/frost growth and the droplet path change due to interaction with the vortices induced by the existing ice shape. It was shown that high level of supersaturation can occur due to the forced and transient response of the relative humidity field to the sudden appearance of new conditions. So the conditions in the suction areas are suitable for a frost growth, which can degrade the performance and may form the substrate for downstream ice growth by working in concert with other mechanisms. For a particular case under stationary conditions, given enough time, relative humidity could increase the LWC as much as 100% or decrease it 30%. However, the time scales over a wing leading edge are much smaller than the scales required by relative humidity effects. Therefore, a portion of the full effect is going to be seen on the exposed surfaces. In a sample case, an estimated 0.4-mm increase in the thickness of the surface roughness was calculated over a 30 min period.

As far as the interaction between roughness-induced vortices and the droplets, it was shown that the unsteady vortex field can severely impact the paths followed by the droplets and cause impingements beyond the direct-impingement region. However, only a certain range of droplets can end up with an impingement with the airframe surface. This is due to their relative inertia; they must have low enough inertia to be able to get into interaction with the vortices, and high enough inertia to penetrate through the high-momentum regions of a shed vortex. For a particular case, up to 6.5% increase in the number of impingements was determined from the droplet tracing in the unsteady flow. For the same particular case, the extra impingements led to 0.24-mm-thick extra liquid-water accumulation in the nonimpingement areas.

It should be noted that the contribution of these mechanisms to the primary ice shape is minor compared with the direct-impingement mechanisms. However, what puts these mechanisms into consideration is that they form the basis for downstream ice accretion, which provides the ground for the growth of ice on surfaces that are either not protected or not exposed to direct impingement due to the primary ice-shape features. Both the relative-humidity-related mechanism and the vortex-interaction mechanism are consistent with the idea that the ice shape has an impact on its own growth. These two mechanisms need further experimental and numerical verification to better establish their significance on the in-flight icing.

Appendix: Supplemental Equations

Governing Equations

The governing equations after the necessary transformations for this study are given next: the vorticity transport equation and the definition of vorticity. In these equations, Ω stands for the vorticity; Ψ and ψ_{inv} stand for the viscous and inviscid component of the stream function, respectively; t and τ stand for real and pseudo time steps, respectively; and f stands for the perturbation geometry, be it an airfoil or ice accretion, from the base geometry, which is a parabola.

$$\begin{aligned}\Omega_\tau + h^2\Omega_t + \bar{\xi}_\xi\bar{\eta}_\eta[\Psi_{\bar{\eta}}\Omega_{\bar{\xi}} - \Psi_{\bar{\xi}}\Omega_{\bar{\eta}}] + (\psi_{\text{inv}})_{\eta'}\bar{\xi}_\xi\Omega_{\bar{\xi}} \\ - f_\xi(\psi_{\text{inv}})_{\eta'}\bar{\eta}_\eta\Omega_{\bar{\eta}} - (\psi_{\text{inv}})_{\xi'}\bar{\eta}_\eta\Omega_{\bar{\eta}} = Re^{-1}\{\bar{\xi}_{\xi\xi}\Omega_{\bar{\xi}} + (\bar{\xi}_\xi)^2\Omega_{\bar{\xi}\bar{\xi}} \\ - f_{\xi\xi}\bar{\eta}_\eta\Omega_{\bar{\eta}} - 2f_\xi\bar{\xi}_\xi\bar{\eta}_\eta\Omega_{\bar{\xi}\bar{\eta}} + [1 + (f_\xi)^2]\bar{\eta}_{\eta\eta}\Omega_{\bar{\eta}} \\ + [1 + (f_\xi)^2](\bar{\eta}_\eta)^2\Omega_{\bar{\eta}\bar{\eta}}\}\end{aligned} \tag{A1}$$

$$\begin{aligned}\bar{\xi}_{\xi\xi}\Psi_{\bar{\xi}} + (\bar{\xi}_\xi)^2\Psi_{\bar{\xi}\bar{\xi}} - f_{\xi\xi}\bar{\eta}_\eta\Psi_{\bar{\eta}} - 2f_\xi\bar{\xi}_\xi\bar{\eta}_\eta\Psi_{\bar{\xi}\bar{\eta}} + [1 + (f_\xi)^2]\bar{\eta}_{\eta\eta}\Psi_{\bar{\eta}} \\ + [1 + (f_\xi)^2](\bar{\eta}_\eta)^2\Psi_{\bar{\eta}\bar{\eta}} = -h^2\Omega + \Psi_\tau\end{aligned} \tag{A2}$$

Box Model Simulation

The steps for the unit-volume-box model simulation are as follows:

1) Specify a time step for integration (e.g., 0.1 s).

2) Find the total number of droplets, N, in the unit volume of air:

$$N = \frac{(\text{LWC}/\rho_{\text{water}})}{(4/3)\pi(\text{MVD}/2)^3} \tag{A3}$$

3) For the given initial temperature (before the impulsive start), get the saturation vapor pressure e^*:

$$e^* = 6.112\exp\left(\frac{17.67T}{T + 243.5}\right) \tag{A4}$$

where temperature is in Celsius. The air is at 100% relative humidity with respect to liquid water initially, and so $e_{\text{initial}} = e^*$.

4) Calculate the imposed temperature using the isentropic relation:

$$\left(\frac{T}{T_{\text{initial}}}\right) = \left(\frac{P}{P_{\text{initial}}}\right)^{\frac{\gamma-1}{\gamma}} \tag{A5}$$

5) Calculate the saturation vapor pressure for new conditions e^*_{new} using Eq. (A4).

6) Update the relative humidity value by

$$\text{RH}_w = e/e^* \tag{A6}$$

7) Update the radii r of the droplets using the following equation:

$$\frac{\mathrm{d}r}{\mathrm{d}t} = \frac{c}{r} \tag{A7}$$

where

$$c = \frac{\text{RH}_w - 1}{[(L/R_vT) - 1](L\rho_{\text{water}}/KT) + (\rho_{\text{water}}R_vT/De^*)}$$

8) To find the change in the LWC, multiply the volume change of a droplet by the density of water and by the number of droplets in the control volume:

$$\Delta\text{LWC} = \Delta V_{\text{droplet}}\rho_{\text{water}}N = \tfrac{4}{3}\pi(r^3 - r_o^3)\rho_{\text{water}}N \tag{A8}$$

9) Then update the LWC and the vapor water content (VWC); obviously, ΔLWC and ΔVWC are equal in magnitude but have opposite signs.

$$\begin{aligned}\text{LWC}_{\text{new}} &= \text{LWC}_{\text{old}} + \Delta\text{LWC} \\ \text{VWC}_{\text{new}} &= \text{VWC}_{\text{old}} + \Delta\text{VWC}\end{aligned} \tag{A9}$$

10) Update the temperature using the latent heat release:

$$\Delta T = \frac{L\Delta \mathrm{LWC}}{(mC_p)_{\mathrm{air}}} \tag{A10}$$

11) Update the volume using the ideal gas equation:

$$\Delta V = \frac{m_{\mathrm{air}} R_{\mathrm{air}}}{p} \Delta T \tag{A11}$$

12) $\mathrm{VWC}_{\mathrm{new}} = \rho_v$, and so using this vapor density, calculate the new value of the vapor pressure e:

$$e = \frac{wp}{0.622 + w} \tag{A12}$$

where $w = \rho_v / \rho_{\mathrm{air}}$.

13) March in time by following steps 5–12 until the LWC and VWC do not change significantly and a new equilibrium is reached.

Derivation of the Velocity Components

The derivation of the velocity components involves the stream function used in the transformed plane. The closed-form formula for the velocity components is

$$\boldsymbol{V} = \nabla\psi \times \hat{k} \tag{A13}$$

where

$$\nabla = \frac{1}{h}\left(\frac{\partial}{\partial \xi'}\hat{e}_{\xi'} + \frac{\partial}{\partial \eta'}\hat{e}_{\eta'}\right) \qquad h = \sqrt{\xi'^2 + \eta'^2}$$

Because the coordinate transformation does not operate in the z direction, the $\hat{k}$ unit vector remains the same. The velocity components in Eq. (4) are then obtained from the cross product given in the preceding expression. As far as the magnitudes that are mentioned in Eq. (6), partial derivatives of the x–y coordinates are used based on the transformation functions given in Eq. (5).

$$V_x = \frac{\partial x}{\partial t} = \frac{\partial x}{\partial \xi'}\frac{\partial \xi'}{\partial t} + \frac{\partial x}{\partial \eta'}\frac{\partial \eta'}{\partial t} = \frac{\partial x}{\partial \xi'}V_{\xi'} + \frac{\partial x}{\partial \eta'}V_{\eta'} = \xi' V_{\xi'} - \eta' V_{\eta'} \tag{A14}$$

$$V_y = \frac{\partial y}{\partial t} = \frac{\partial y}{\partial \xi'}\frac{\partial \xi'}{\partial t} + \frac{\partial y}{\partial \eta'}\frac{\partial \eta'}{\partial t} = \frac{\partial y}{\partial \xi'}V_{\xi'} + \frac{\partial y}{\partial \eta'}V_{\eta'} = \eta' V_{\xi'} + \xi' V_{\eta'} \tag{A15}$$

$$V_x^2 + V_y^2 = (\xi'^2 V_{\xi'}^2 + \eta'^2 V_{\xi'}^2) + (\xi'^2 V_{\eta'}^2 + \eta'^2 V_{\eta'}^2) = h^2 (V_{\xi'}^2 + V_{\eta'}^2) \tag{A16}$$

And Eq. (A16) leads to Eq. (6).

Acknowledgments

Technical tasks described in this document include tasks supported with shared funding by the United States rotorcraft industry and the Government under the Rotorcraft Industry Technology Association (RITA)/NASA cooperative agreement number NCC2-9019, Advanced Rotorcraft Technology, 01 January 2001. The authors also would like to thank David Lewellen for his continued guidance during this study.

References

[1] Potapczuk, M. G., "A Review of NASA Lewis' Development Plans for Computational Simulation of Aircraft Icing," AIAA Paper 99-0243, Jan. 1999.

[2] Santos, L. C. C., Neto, L. T., Papa, R., Oliveira, G. L., Jesus, A. B., and Wirogo, S., "Grid Sensitivity Effects in Collection Efficiency Computation," AIAA Paper 2004-0566, Jan. 2004.

[3] Tan, C., "A Tentative Mass Loss Model for Simulating Water Droplet Splash," AIAA Paper 2004-0410, Jan. 2004.

[4] Reehorst, A. L., Ratvasky, T. P., and Sims, J., "Close-Up Analysis of In-Flight Ice Accretion," NASA TM-106457, 2004.

[5] Wright, B. W., "User Manual for the NASA Glenn Ice Accretion Code LEWICE," NASA CR-209409, 1999.

[6] Ogretim, E., Huebsch, W., and Narramore, J., "The Effects of Leading-Edge Ice Roughness on Downstream Frost Formation," AIAA Paper 2004-0059, Jan. 2004.

[7] Ogretim, E., and Huebsch, W. W., Narramore, J., and Mullins, B., "Mechanisms for Downstream Ice Growth," *SAE 2005 Transactions: Journal of Aerospace*, 2006, pp. 1212–1219.

[8] Huebsch, W. W., and Rothmayer, A. P., "Effects of Surface Ice Roughness on Dynamic Stall," *Journal of Aircraft*, Vol. 39, No. 6, 2002, pp. 945–953.

[9] Ogretim, E., and Huebsch, W., "A Novel Method for Automated Grid Generation of Ice Shapes for Local-Flow Analysis," *International Journal for Numerical Methods in Fluids*, Vol. 44, No. 6, 2004, pp. 579–597.
doi:10.1002/fld.659

[10] White, F. M., *Viscous Fluid Flow*, 2nd ed., McGraw–Hill, New York, 1991, p. 182.

[11] Rogers, R. R., *A Short Course in Cloud Physics*, 2nd ed., Pergamon, New York, 1979, p. 24.

[12] XFOIL, Software Package, Ver. 6.94, Massachusetts Inst. of Technology, Cambridge, MA, 18 Dec. 2001.

[13] Davis, R. T., Ghia, U., and Ghia, K. H., "Laminar Incompressible Flow Past a Class of Blunted Wedges Using the Navier-Stokes Equations," *Computers and Fluids*, Vol. 2, No. 2, Aug. 1974, pp. 211–223.
doi:10.1016/0045-7930(74)90015-2

[14] Bragg, M. B., "Rime Ice Accretion and its Effect on Airfoil Performance," NACA CR-165599, 1982.

[15] Dompierre, J., Cronin, D. J., Bourgault, Y., Baruzzi, G., Habashi, W. G., and Wagner, G. A., "Numerical Simulation of Performance Degradation of Ice Contaminated Airfoils," AIAA Paper 1997-2235, June 1997.

[16] *Validation Report for LEWICE 2.0* [CD-ROM], NASA CR 208690, Jan. 1999.